THE FLOW OF A FALLING ELLIPSE: NUMERICAL METHOD AND CLASSIFICATION

R.-J. Wu S.-Y. Lin*

Department of Aeronautics and Astronautics
National Cheng Kung University
Tainan, Taiwan

ABSTRACT

A modified direct-forcing immersed-boundary (IB) pressure correction method is developed to simulate the flows of a falling ellipse. The pressure correct method is used to solve the solutions of the two dimensional Navier-Stokes equations and a direct-forcing IB method is used to handle the interaction between the flow and falling ellipse. For a fixed aspect ratio of an ellipse, the types of the behavior of the falling ellipse can be classified as three pure motions: Steady falling, fluttering, tumbling, and two transition motions: Chaos, transition between steady falling and fluttering. Based on two dimensionless parameters, Reynolds number and the dimensionless moment of inertia, a Reynolds number-inertia moment phase diagram is established. The behaviors and characters of five falling regimes are described in detailed.

Keywords: Falling ellipse, Pressure correction method, Fluttering, Tumbling.

1. INTRODUCTION

The motion of a two-dimensional falling ellipse is complicated and beautiful. This is due to the coupling of forward motion to lateral oscillations by the surrounding fluid. It can be characterized by six parameters: The major and minor semi-axes, the densities of the ellipse and fluid, the kinematic viscosity of the fluid, and the gravitational acceleration. From these parameters, three dimensionless parameters, Reynolds number Re, the dimensionless moment of inertia I^*, and aspect ratio of the ellipse e, are obtained to classify the behaviors of the falling ellipse. Generally, the types of the behaviors of a falling ellipse can be classified as three pure motions: Steady falling, fluttering, tumbling, and two transition motions: Chaos, transition between steady falling and fluttering. Recently, many researchers have been investigated the motion of the falling ellipse [1-5]. Tanabe and Kaneko [6] proposed a simple model for a falling paper. They assumed the paper is subjected to three forces: Lift, friction, and gravity. They can reproduce qualitatively the tumbling, fluttering, and chaos motions. Belmonte *et al*. [7] modified Tanabe and Kaneko's model to include lift, gravity, and inertial drag to describe the tumbling and fluttering motions. They also presented a simple laboratory on flat strips dropped in a quasi-2D geometry and observed two fundamental motions: Side-to-side oscillation (flutter) and end-over-end rotation (tumble). Mahadevan *et al*. [8] showed experimentally that the tumbling frequency Ω of a card of length l, width w and thickness d ($l >> w >> d$) scales as $\Omega \sim d^{1/2}w$. Pesavento and Wang [9] investigated the problem of a falling paper by solving the two dimensional Navier-Stokes equations subject to the motion of a free-falling body at Reynolds numbers around 1000. They found that the aerodynamic lift on a tumbling plate is dominated by the product of linear and angular velocities rather than velocity squared, as appropriate for an airfoil. Mittal *et al*. [30] have also studied the free falling motion of a rectangular plate, and the value of I^* is kept greater than 0.17 for all cases in their simulations. Their phase plot (thickness ratio versus Reynolds number) indicate that the tendency to tumble increases with Reynolds number and decreasing thickness ratio, and there is a maximum thickness ratio (about 0.6) which the plate would not auto-rotate for any Reynolds number.

Here we develop a modified direct-forcing immersed-boundary (IB) pressure correction method to solve the two dimensional Navier-Stokes equations subject to the motion of a free-falling ellipse and investigate its behaviors. A small fixed aspect ratio ($e = 0.125$) is used to simplify the discussion and prevent that the tumbling motion disappears for all Reynolds number. Based on two dimensionless parameters, Reynolds number and the dimensionless moment of inertia (Re and I^*), a Re – I^* phase diagram is established to classify the falling behavior. In borderline cases, the initial incline angle θ_0 is likely to influence its falling motion and produce different average falling velocity. Especially in the chaos case, the sample av-

* Corresponding author (sylin@mail.ncku.edu.tw)

DOI : 10.1017/jmech.2015.47
Copyright © 2015 The Society of Theoretical and Applied Mechanics, R.O.C.
https://doi.org/10.1017/jmech.2015.47 Published online by Cambridge University Press

erage range of the mean velocity is hard to determine due to its aperiodicity. Rather than the mean velocity, the terminal velocity u_t introduced in section 4 is a reasonable choice characteristic velocity when determining Reynolds number. These two parameters (Re and I^*) directly determine the viscous force and the rotational energy, respectively. Based on the conclusion of Mittal *et al*. [30], most of the moment is from the surface pressure and not the shear stress. For the low-Re regimes, the falling behavior is dominated by the viscous force, and the steady falling only occurs. At high enough Re, the falling behavior is dominated by the rotational motion, then the tumbling and fluttering take place.

The task of developing numerical methods used to simulate fluid-particle interaction flows is a challenging task, and there is also a need for understanding many physical phenomena involved in these flow problems. A fluid-particle interaction flow involves many kinds of interactions, such as fluid-fluid, particle-particle, and fluid-particle interactions. The corresponding physical problems include two-phase, solid-fluid mixture, and sedimentation flow problems. The needed methods are to track the interface positions between two phases and to compute the interaction forces between a fluid and a particle. Here the fluid-particle interaction problems are considered.

There are several methods available for fully resolved simulation of particulate flows. Haeri and Shimpton gave a nice review paper [10]. They classified the methods into two general categories based on the treatment of underlying mesh namely fixed mesh methods and body-conformal mesh methods. Hu [11] and Johnson and Tezduyar [12,13] have developed finite element methods with moving boundary grid system. Hu *et al*. [14] and Gan *et al*. [15] simulated particle motions using ALE technique. Haeri and Shimpton [10] pointed out that the flow solver, mesh movement, and remeshing techniques are main features of a body- conformal mesh method. Specially, one shall put a significant effort for simulating the flow of many particle motions [16]. Alternatively, the fixed mesh methods can save computational costs on the mesh movement and remeshing. The fixed mesh methods can be categorized into two subcategories namely IB methods and fictitious domain (FD) methods. FD methods consist of a large class of solutions techniques on partial differential equation for handling flow-particle interaction in a large but simpler domain (Friction Domain) [17,18]. On the other hand, the IB methods introduce an immersed boundary force density for capturing a particle motion. Generally speaking, the immersed boundary force density is modulated by a linear spring relation due to the displacement between a boundary point and a computational point at a solid boundary [19-22]. This method needs to determine the stiffness coefficient. In practice, this coefficient is often dependent on the problem, which can lead to severe restrictions on the time step [23]. The other methods compute the force density at the particle boundary by asking the velocity on the immersed Lagrangian boundary points be equal to the velocity of the particle [24,25]. It needs an approximation of the delta function to transform the force density on the boundary points to flow elements. To avoid complicated interpolations and transformations of the force density on the boundary points to flow elements, a direct forcing method is introduced in this paper [26]. Here, a modified version to our original direct-forcing IB pressure correction method [27] is developed.

The paper is organized as follows: A modified direct -forcing immersed-boundary pressure correction method is introduced in Section 2. The volume integral for evaluating the hydrodynamic forces are given. In Section 3, two numerical test cases, the flow past a fixed ellipse and the flow with a falling ellipse, are performed to demonstrate the accuracy of the proposed numerical method. Flow simulations of a falling ellipse and its classifications are shown in Section 4. Finally, conclusions are given in Section 5.

2. NUMERICAL METHODS

In this section, a modified direct-forcing immersed-boundary pressure correction method is introduced. This method is a modified version of the direct-forcing IB pressure correction method introduced in our paper [27]. The volume integral for evaluating the hydrodynamic forces are given. An algorithm for simulating the particulate flows is presented.

2.1 Modified Direct-Forcing IB Pressure Correction Method

The incompressible Navier-Stokes equations of a laminar flow can be written as

$$\frac{\partial}{\partial x_j}(u_j) = 0 \tag{1a}$$

$$\frac{\partial u_i}{\partial t} + \frac{\partial}{\partial x_j}(u_i u_j) + \frac{\partial p}{\partial x_i} - \nu\nabla^2 u_i = S_i \tag{1b}$$

where $\vec{u} = (u_1, u_2, u_3)$ is the velocity and p the pressure. S_i represents some sources applied in the momentum equations. The pressure correction method has the following structures: at the time step t^n

1. Predictor step: Compute $\vec{u}^*$ by using $\vec{u}^n$ and p^n, as below:

$$\left(\frac{1}{\Delta t} - A_0\right)u_i^* = H_i(\vec{u}^*) - \Delta_i p^n + \frac{u_i^n}{\Delta t} + S_i \tag{2a}$$

where

$$A_0 u_i^* + H_i(\vec{u}^*) \approx -\frac{\partial}{\partial x_j}(u_i^* u_j^*) + \nu\nabla^2 u_i^* \tag{2b}$$

We use a second-order upwind finite volume method to discretize the convection operators and the second-order central difference method to discretize the diffu-

https://doi.org/10.1017/jmech.2015.47 Published online by Cambridge University Press

sion operators. For the details of the coefficient A_0 and the operator $H_i()$, please see our paper [27]. Here the modified direct-forcing IB pressure correction method is introduced. First, to consider the motion of a particle moving in a fluid, an index function, ϕ_p, is defined to identify the body cell ($\phi_p = 1$) in the particle, the fluid cell ($\phi_p = 0$) and the interface cell ($0 < \phi_p < 1$). For example, the index function can be defined as

$$\phi_P(\vec{x}) = \begin{cases} 1, & \vec{x} \in P \\ 0, & \vec{x} \notin P \end{cases} \tag{3}$$

Assume the velocity of the particle is $\vec{U}_P$, then, in the body cell, Eq. (2) becomes

$$\frac{U_{P,i}}{\Delta t} - A_0 u_i^* = H_i(\vec{u}^*) - \Delta_i p^n + \frac{u_i^n}{\Delta t} + S_i \tag{4}$$

We combine Eqs. (2) and (4), (2) − ϕ_p·(4), and modify Eq. (2) to

$$(1-\phi_P)\left[\left(\frac{1}{\Delta t} - A_0\right)u_i^* - H_i(\vec{u}^*) + \Delta_i p^n - \frac{u_i^n}{\Delta t} - S_i\right] + \phi_P\left[\frac{u_i^* - U_{P,i}}{\Delta t}\right] = 0 \tag{5}$$

Then Eq. (5) is solved to obtain $\vec{u}^*$ instead of Eq. (2). From Eq. (5), it can be seen that no forcing term is applied in the fluid cell and the velocity $\vec{u}^* = \vec{U}_P$ in the body cell. To avoid errors induced by the matrix solver, the following projection operator is used:

$$\vec{u}^*(\vec{x}) = \left(1-\phi_P(\vec{x})\right)\vec{u}^* + \phi_P(\vec{x})\,\vec{U}_P \tag{6}$$

This operator can make sure that the velocity $\vec{u}^* = \vec{U}_P$ in the body cell. In the origin pressure correction method, it uses Eqs. (2) and (6) to obtain the predictor velocity [27]. Here the modified method uses Eqs. (5) and (6) to obtain the predictor velocity. We think this modification shall produce more accurate velocity fields in the unsteady flow computations, since Eq. (5) considers the motion of the moving particle more straightforward.

2. Corrector step: To derive a pressure-velocity coupling which satisfies conservation of mass is the goal of this step. Equation (5) is replaced by the following form to solve the velocity and pressure, $\vec{u}^{n+1}$, p^{n+1}, as:

$$(1-\phi_P)\left[\left(\frac{1}{\Delta t} - A_0\right)u_i^{n+1} - H_i(\vec{u}^*) + \Delta_i p^{n+1} - \frac{u_i^n}{\Delta t} - S_i\right] + \phi_P\left[\frac{u_i^{n+1} - U_{P,i}}{\Delta t}\right] = 0 \tag{7}$$

Subtracting Eq. (7) from (5) and then taking the divergence of the resulting, the implicit pressure correction equation for the first corrector step is given by

$$\nabla\cdot(B\nabla\psi) = \nabla\cdot\vec{u}^* \tag{8}$$

where $\psi = p^{n+1} - p^n$, $B = \left(\frac{1}{\Delta t} - A_0\right)^{-1}$.

And u^{n+1}, p^{n+1} are givens as

$$\begin{aligned} p^{n+1} &= p^n + \psi \\ \vec{u}^{n+1} &= \vec{u}^* - B\nabla\psi \end{aligned} \tag{9}$$

In this proposed method, all variables are located at the centre of each grid cell. To stabilize the above Poisson equation and to avoid the checker-board pressure, the following modified equation is solved instead of using Eq. (8):

$$\nabla\cdot(B\nabla\psi) - \varepsilon_C\psi = \nabla\cdot\vec{u}^* + \varepsilon_D\left(\frac{\partial^4 p^n}{\partial x^4}\Delta x^2 + \frac{\partial^4 p^n}{\partial y^4}\Delta y^2\right) \tag{10}$$

Here, ε_C and ε_D are small nonnegative constants. From theoretical point of view, the term $\varepsilon_C\psi$ stands for adding some compressibility effect on the fluid system as the weakly compressibility model did. After a series of numerical experiments, we find out that the chosen value of ε_C between 0 and 0.1 did not affect the accuracy of the present method. Moreover ε_C = 0.1 can speed up the convergence rate in our numerical experiments. The value of ε_D actually depends on the reference velocity. As the reference velocity is normalized to be equal to 1, then ε_D can be chosen as

$$\varepsilon_D = (0.1 \sim 0.01)\cdot\Delta x^2 \tag{11}$$

The choice of ε_D can produce a fourth-order truncation error in the modified Poisson equation, and doesn't affect the accuracy of the proposed pressure correction method.

2.2 Hydrodynamic Forces

Generally, the hydrodynamic forces acting on the particle is computed by integrating the fluid stress over the particle surface. By applying the Gauss theorem, the surface integral can be transformed into a volume integral. Then the hydrodynamic force acting on the particle is obtained by

$$\vec{F} = \sum_{\Omega}\phi_P\Delta V(-\nabla p + \mu\nabla^2\vec{u}). \tag{12}$$

where the summation is taken in the whole computational domain, Ω, and ΔV is the volume of each mesh. The volume integral makes our numerical method easier to implement, specially, in the simulation of a moving particle. By a similar way, the torque on a particle is computed by the following expression:

$$\vec{T} = \sum_{\Omega}\phi_P\Delta V\left[(\vec{x} - \vec{X}_C)\times(-\nabla p + \mu\nabla^2\vec{u})\right] \tag{13}$$

https://doi.org/10.1017/jmech.2015.47 Published online by Cambridge University Press

where $\vec{X}_C$ is the center of mass of the particle. About the accuracy of these two force evaluations, please see our paper [27].

2.3 Implementation of Modified Direct-Forcing IB Pressure Correction Method

The modified direct-forcing pressure correction method is implemented in two- and three-dimensional particulate flows. The first issue is how to determine the index function ϕ_p. One can use the signed distance function, ϕ_S, which equals to the shortest distance with a sign of the grid point to the particle. It is defined as $\phi_S > 0$ when the point is outside the particle. Then the volume fraction function, ϕ_p, can be defined to identify the body cells ($\phi_p = 1$) in the particle, the fluid cell ($\phi_p = 0$) and the interface cell ($0 < \phi_p < 1$). The range of interface cells will determine the accuracy of the particle surface and the smoothness of the numerical method.

Let $\vec{u}(\vec{x}, t^n)$ and $p(\vec{x}, t^n)$ be the velocity and pressure of the flow and $\vec{U}^{P,n}$, $\vec{X}^{P,n}$, $\vec{F}^{P,n}$, $\vec{T}^{P,n}$ the particle velocity, position, total particle force, and torque of the particle P, respectively. Their values are known at the current time step, $t = t^n$. First, by using the following ordinary equations, $\vec{U}^{P,n+1}$, $\vec{X}^{P,n+1}$, $\vec{\omega}^{P,n+1}$ at $t = t^{n+1}$ can be computed:

$$\frac{d\vec{U}^p}{dt} = \vec{F}^p, \quad \frac{d\vec{X}^p}{dt} = \vec{U}^p, \quad I\frac{d\vec{\omega}^p}{dt} = \vec{T}^p \tag{14}$$

where I is the inertia matrix of the particle. The explicit Euler method is used to solve the system of ordinary differential equations (14). From the new position $\vec{X}^{P,n+1}$ of the particle P, the updated index function ϕ_p at the time step, $t = t^{n+1}$, is defined. Then, the predicted velocity, $\vec{u}^*$, is obtained by Eqs. (6) and (7). Finally, the velocity and pressure at the time step, $t = t^{n+1}$, are obtained by Eq. (9).

The total force acting on a particle includes the gravity/buoyancy force and hydrodynamic force. Hence the total force acting on the particle can be written as follows:

$$\vec{F}^p = \left(1 - \frac{\rho_f}{\rho_s}\right) M^p \vec{g} + \vec{F} \tag{15}$$

where M^p is the mass of the particle and $\vec{F}$ obtained by Eq. (12) is the hydrodynamic force acting on the particle.

We now present the modified direct-forcing IB pressure correction method as follows:

Algorithm: Modified Direct-forcing IB pressure correction method

Step 1: At t^n, $u(\vec{x}, t^n)$, $p(\vec{x}, t^n)$, $\vec{U}^{P,n}$, $\vec{X}^{P,n}$, $\vec{F}^{P,n}$, and $\vec{T}^{P,n}$ are known.

Step 2: Using Eq. (14), compute $\vec{U}^{P,n+1}$, $\vec{X}^{P,n+1}$ and $\vec{\varpi}^{P,n+1}$ at $t = t^{n+1}$.

Step 3: Determine the volume fraction function, ϕ_p, for the particle.

Step 4: Using the predicted step, Eqs. (5) and (6), compute $\vec{u}^*$.

Step 5: Using the corrector step, Eq. (10), compute ψ. Then using Eq. (9), compute $\vec{u}^{n+1}$ and p^{n+1}.

Step 6: Using Eqs. (12) and (13), compute the forces $\vec{F}^{P,n+1}$ and $\vec{T}^{P,n+1}$.

Step 7: Advance one time step and return to Step 2.

3. NUMERICAL TESTS

Two numerical test cases, the flow past a fixed ellipse and the flow with a falling ellipse, are performed to demonstrate the accuracy of the proposed numerical method. The grid independence is also checked.

3.1 Flow Past a Fixed Ellipse

In this section we consider the two-dimensional flow past a fixed ellipse. The ellipse has major and minor axis of lengths $2a$ and $2b$ respectively. e is the aspect ratio defined as $e = b/a$. The ellipse is assumed to be immersed in a uniform flow with a velocity U and an angle of attack α. Re is the Reynolds number defined as $\mathrm{Re} = 2Ua/v$, v is the kinematic viscosity.

A non-uniform Cartesian grid used in the simulations. The grid points are clustered around the ellipse. In the immersed boundary region that embeds the ellipse a uniform mesh of equal resolution along all two directions is used ($\Delta x = \Delta y = 1$).

This high resolution region extends over the subdomain, $[-2.5a, 2.5a]^2$. Outside of this region, a geometric stretching is used. The overall grid resolution used for the finest grid system in this simulation is up to 320 × 320 points. Figure 1 shows the stretched grid system around the ellipse. For the boundary conditions, the inflow and outflow boundary conditions are used in the x-direction. The non-slip boundary condition is used at the y-direction. The index function can be defined as:

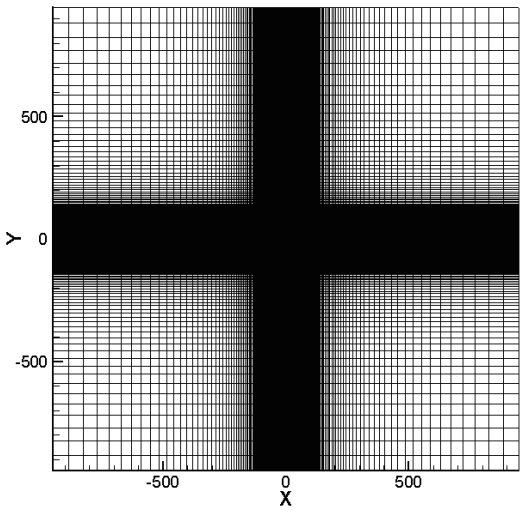


Fig. 1 The stretched grid system around the ellipse.

https://doi.org/10.1017/jmech.2015.47 Published online by Cambridge University Press

$$\phi_P(x,y)=\begin{cases}1, & (x/a)^2+(y/b)^2\le 1\\ 0, & \text{otherwise}\end{cases} \tag{16}$$

First we establish the number of grid needed for a semi-major axis, a, of an ellipse in order to achieve adequate resolution of the ellipse. The particular case considered is characterized by $U = 0.1$, Re = 40, and $e = 0.1$, $\alpha = 0$. Four different levels of resolution are used (a = 20, 30, 40, 50). The drag coefficients for the different simulations are presented in Table 1. The finest grid results as taken to be the baseline and percentile difference finest and the coarse grids defined as difference $=\left|C_{D,\text{coarse}}-C_{D,\text{finest}}\right|/C_{D,\text{finest}}\times 100\%$ are presented. C_D is the drag coefficient defined as:

$$C_D=\frac{F_x}{\rho_f U^2 a} \tag{17}$$

where F_x is the hydrodynamic force in x-component.

Based on the above results, the bulk of the results to be presented (unless otherwise stated) are obtained with a resolution of $a = 40$. Table 2 shows the drag coefficients for a series of test. It shows that the computational results are compared well with the known data [28,29].

4. FLOW SIMULATIONS OF A FALLING FLAT PLATES

In this section, the flow with a falling flat plate is investigated. A freely falling flat plate is characterized by six parameters: The major and minor semi-axes, a and b, the density ρ_s of the flat plate, the density ρ_f of the fluid, the kinematic viscosity ν of the fluid, and the gravitational acceleration g. Following the same definition used in [1], these six parameters can be simplified as three non-dimensional numbers:

Table 1 Grid resolution test for the flow past a fixed ellipse with the case of $e = 0.1$, $U = 0.1$ and Re = 40.

a	b	Grid	Domain	C_D	Difference
20	2	188 × 188	$[-20a, 20a]^2$	0.695	1.257%
30	3	248 × 248	$[-20a, 20a]^2$	0.700	0.502%
40	4	304 × 304	$[-20a, 20a]^2$	0.702	0.233%
50	5	360 × 360	$[-20a, 20a]^2$	0.704	–

Table 2 The comparisons of drag coefficients. "Present" means the drag coefficient obtained by the proposed method.

Method	Re	e	C_D / Present	
Dennis & Chang [28]	40	0.1	0.716	0.702
Dennis & Chang	40	0.2	0.794	0.792
Dennis & Chang	40	0.4	0.964	0.983
Lugt & Haussling [29]	200	0.1	0.275	0.284
Lugt & Haussling	50	0.1	0.695	0.616

1. The aspect ratio of the ellipse, $e = b/a$;
2. The dimensionless moment of inertia, $I^* = I_s / I_f$, where I_s is the moment of inertia per length about the axis of symmetry of the flat plate and $I_f = \pi\rho_f a^4/2$ is the moment of inertia per length about the axis of symmetry of a cylinder.
3. The Reynolds number, $\mathrm{Re} = 2au_t/\nu$, where $u_t=\sqrt{(\rho_r-1)gA/a}$ is the terminal velocity estimated by balancing gravity against the fluid force on a plate of size $2a$ with the drag coefficient equal to 1, $\rho_r = \rho_s/\rho_f$ is the density ratio and A is the cross-section area of the flat plate.

About the cross-section shape of the flat plates, we use rectangle and ellipse, and gather its related parameter in Table 3.

According to these three parameters, the dynamic behavior of the ellipse falling with the gravity force can be classified into three pure motions: steady falling, fluttering, and tumbling. Based on the above section, the non-uniform Cartesian grid system with 304 × 304 points and $a = 40$ is used in this simulation. Here the aspect ratio e is fixed to be 0.125. Initially, both the fluid and plate are stationary. The plate will be falling derived by the gravity force and its falling trajectory may be affected by the initial incline angle θ_0.

Table 3 The dimensional moment of inertia I_s and the dimensionless moment of inertia I^* of the rectangular and elliptical plates.

	Rectangle	Ellipse
A	$4ab$	πab
u_t	$\frac{4}{3}\rho_s ab(a^2+b^2)$	$\frac{\pi}{4}\rho_s ab(a^2+b^2)$
I^*	$\frac{8}{3\pi}\rho_r e(1+e^2)$	$\frac{1}{2}\rho_r e(1+e^2)$

Table 4 Experimental and numerical falling rectangular plate averaged translational and angular velocities. We report the averages of the absolute values of U, V, and Ω.

Rectangle	$\bar{U}$ (cm/s)	$\bar{V}$ (cm/s)	$\bar{\Omega}$ (rad/s)	β (deg)	θ_0 (deg)
Present	16.3	–12.2	15.7	36.7	45
Anderson *et al.* [1]	15.9	–11.5	14.5	35.8	45
Jin and Xu [3]	15.1	–11.8	15.0	37.0	45

Ellipse	$\bar{U}$ (cm/s)	$\bar{V}$ (cm/s)	$\bar{\Omega}$ (rad/s)	β (deg)	θ_0 (deg)
Present	14.9	–8.8	18.8	30.6	42
Anderson *et al.* [1]	15.6	–7.4	18.0	25.3	11.5
Jin and Xu [3]	15.3	–11.2	16.9	36.2	11.5
Kolomenskiy and Schneider [4]	11.3	–7.2	19.4	32.5	11.5

https://doi.org/10.1017/jmech.2015.47 Published online by Cambridge University Press

4.1 Comparison Between Experiment and Simulations

A quasi-two-dimensional experiment of a falling rectangular plate was conducted by Andersen *et al*. [1]. The related numerical simulations including rectangular and elliptical plates are performed by Andersen *et al*. [1], Jin and Xu [3], and Kolomenskiy and Schneider [4]. We perform the same numerical simulation under the same physical parameters: $a = 0.324$ (cm), $b = 0.0405$ (cm), $\rho_f = 1.0$ (g/cm^3), $\rho_s = 2.7$ (g/cm^3), $\nu = 0.0089$ (cm^2/s), and $g = 980$ (cm/s^2). For the rectangular and elliptical plates, we obtain the dimensionless moment of inertia $I^* = 0.29$ and 0.17, and Reynolds numbers Re = 1196 and 1060, respectively. Releasing from the initial angle $\theta_0 = 45°$, the rectangular plate draw a pure tumbling trajectory in Fig. 3. On the other hand, the ellipse plate is easily affected by the initial angle and mix few fluttering behavior into tumbling motion since it locate at the chaotic regime according to its parameters $I^* = 0.17$ and Re = 1060. To obtain the tumbling motion, we set the initial angle as $\theta_0 = 42°$ by trial and error. In Fig. 3, it keeps the tumbling motion for a long time until breaking by the first fluttering motion. About the rectangle and ellipse plates, their averaged translation velocity $(\bar{U}, \bar{V})$, angular speed $\bar{\Omega}$, and initial angle θ_0 are listed in Table 4.

In Figs. 2 and 3, the red circle marked in the falling trajectory indicates the locus of zero vertical velocity. During each tumbling motion, the mass center of a flat plate is elevated to the extremum and its vertical velocity decrease to zero at the same time. Between two red circles, the descent angle of a tumbling motion is computed from slope of the line connecting these two red circles. To compare the trajectory with other research in detail, the decent angle β is defined as the average of all the inclined angles and is also listed in Table 4. For the rectangle plate, the averaged falling velocity, angular speed, and descent angle all match reasonably with experiment of Andersen *et. al*. [1] and simulation of Jin and Xu [3]. For the ellipse plate, our result is very close to the simulations of Andersen *et al*. [1] and Kolomenskiy and Schneider [4]. Comparing with rectangle plate, ellipse plate rotate faster due to smooth geometric shape, but has few velocity in vertical direction at the same time.

4.2 Definition of the Freely Falling Behavior

When a flat plate is falling in a viscous fluid with the gravity force, its dynamic behavior is possibly a pure or periodic motion and sometimes draws a chaotic trajectory. Before analyzing further, we consider how to adequately define this dynamic behaviors under specify conditions. Beside the three dimensionless parameters e, Re and I^* mentioned above, the initial settings of its inclined angle, translation velocity and angular speed also influence its behavior. If the falling behavior is regarded as a dynamic system, the initial angle θ_0 can be used to determine its stability. For unstable system,

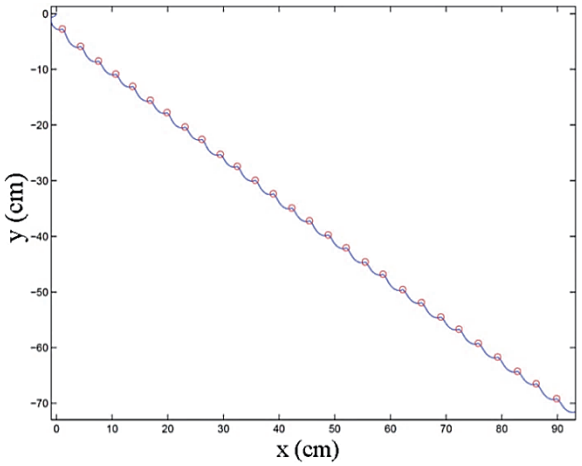


Fig. 2 The tumbling trajectory of the falling rectangular plate.

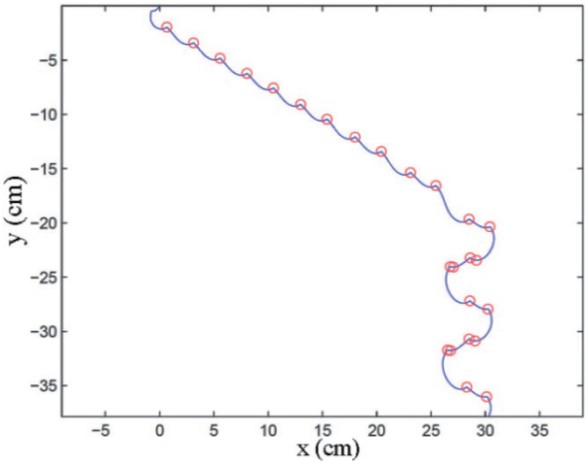


Fig. 3 The falling trajectory of the ellipse plate.

the differential change of the initial angle will be enlarged and influence its falling behavior. Using symmetry, we simply consider three different angle 5°, 45°, 85° to cover the range 0° ~ 90° of the initial angle θ_0. We recognize the dynamic behavior as a pure motion for the same type of pure motion with these three initial angles or a transition motion for not.

4.3 Phase Diagram

Smith [5] established a phase diagram for rectangular plates with chord thick from 0.02 to 0.04. In the phase diagram, the plates falls steadily without any periodic motion when Re is less than 50 ~ 85, depending on I^*, and descend with a slight fluttering motion for higher Re. On the other hand, the plates falls with tumbling motion at high enough Re and I^*, but exhibit fluttering motion without any rotation for I^* less than 0.1 even at high Re. In a quasi-two-dimensional experiment, Belmonte *et al*. [7] found a critical value $I^* = 0.4$ about the transition from fluttering to tumbling. Andersen *et al*. [1] performed four experimental tests for rectangular plates and found that the plate is tumbling at $I^* = 0.48$ ($e = 1/5$), chaos at $I^* = 0.39$ ($e = 1/6$), tumbling at $I^* = 0.29$ ($e = 1/8$), and fluttering at $I^* = 0.16$ ($e = 1/14$).

https://doi.org/10.1017/jmech.2015.47 Published online by Cambridge University Press

Figure 4 plots the phase diagram which shows the dynamical behavior of the ellipse as a function of the two parameters I^* and Re. Using the definition in section 4.2, the phase diagram is divided into three pure motion regimes and two border regimes with different color spots. Red, green, and blue symbols denote the pure motion regimes and represent the fluttering, steady falling and tumbling, respectively. For the border regimes, one is the transition between steady falling and fluttering. It is represented by yellow symbol and has narrow distribution. Another one is the chaotic motion which mixes tumbling motion with fluttering motion irregularly. It is represented by magenta symbols and distribute widely.

From Fig. 4, it is found that the ellipse descends steadily without any periodic motion when Re below 50 ~ 100, depending on I^*. As the Reynolds number increases slightly, the falling behavior enters a narrow transition regime between steady falling and fluttering motion. For approximately horizontal initial angle θ_0, the ellipse has less rotational kinetic energy and falls steadily without any periodic motion. For largely initial angle θ_0, the ellipse falls with enough rotational kinetic energy and a fluttering motion slightly appears. For larger Reynolds number, the falling behavior change from fluttering to tumbling motion and mixes both motions at around $I^* = 0.12 \sim 0.35$, depending on Re. The mixed motion not only appears in this range but also distributes widely around the tumbling motion regime. Although the transition region covers the Smith [5] and the Belmonte *et al*. [7], we think that our two- dimensional results shall be different to their quasi-two-dimensional experiments since the aspect ratio also affects the falling behavior.

In the following subsections, we will describe the behaviors and characters of pure motion regime in detail. Here we would like to demonstrate the general behaviors of five regimes. The trajectories of the ellipse at different parameter settings are shown in Fig. 5 steady falling with Re = 100 and $I^* = 0.08$, Fig. 6 fluttering with Re = 1000 and $I^* = 0.08$, Fig. 7 tumbling with Re = 1000 and $I^* = 0.35$, Fig. 8 chaos with Re = 1000 and $I^* = 0.25$, and Fig. 9 transition between steady falling and fluttering with Re = 100 and $I^* = 0.25$. One can observe two fundamental motions: side-to-side oscillation (flutter) and end-over-end rotation (tumble). Chaos can be seen as a random combination of flutter and tumble. Figures 10, 11 and 12 show the vorticity contours of the steady falling, fluttering and tumbling, respectively. In these contour plots, the vorticity are recalculated in log-scale by the fallowing equation:

$$\omega_{\log} = \begin{cases} \text{sign}(\omega) \times (n + \log_{10} |\omega|), & \text{if } |\omega| > 10^{-n} \\ 0, & \text{otherwise} \end{cases} \quad (18)$$

The minimum absolute value of the vorticity is about 10^{-5} and then n is taken to be 6.

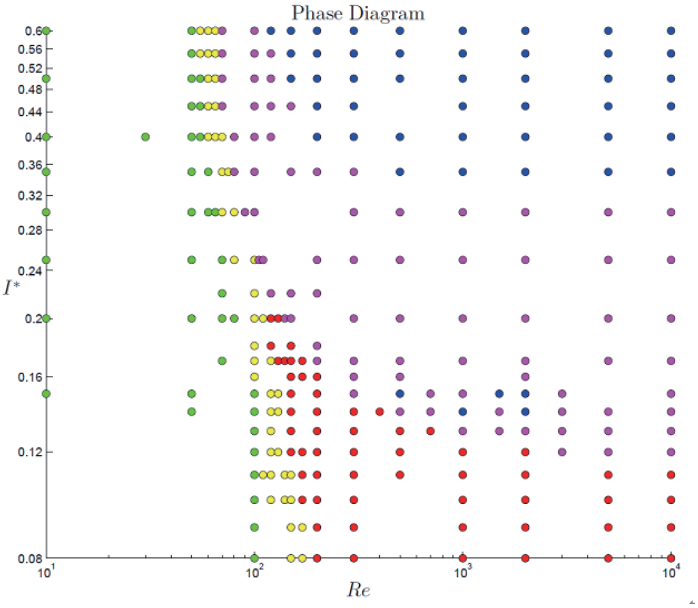


Fig. 4 Phase diagram showing the dynamical behavior of the ellipse as a function of the two parameters, I^* and Re. Green (Regime A), red (Regime B) and blue (Regime C) symbols represent ellipse with steady falling, fluttering, and tumbling behavior, respectively. Yellow (Regime D) symbols represents transition between steady falling and fluttering behavior, and magenta (Regime E) symbols represents transition between fluttering and tumbling behavior.

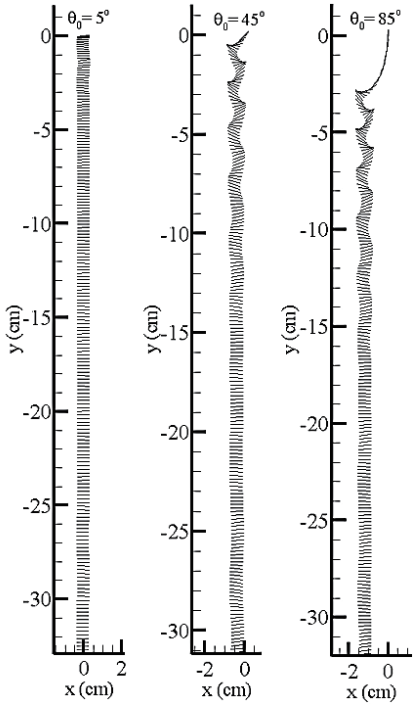


Fig. 5 The trajectories of the ellipse plate at Re = 100 and $I^* = 0.08$.

https://doi.org/10.1017/jmech.2015.47 Published online by Cambridge University Press

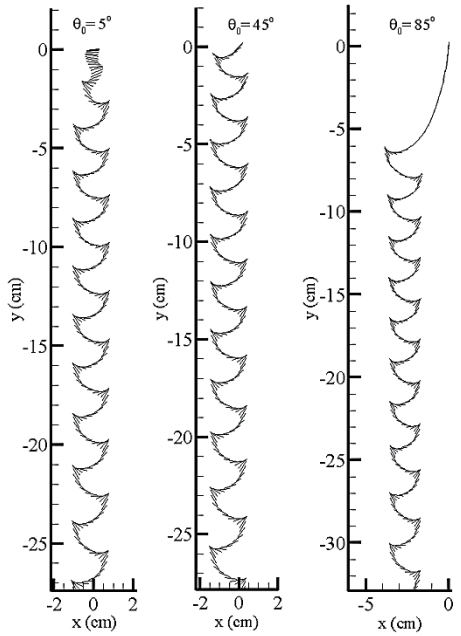


Fig. 6 The trajectories of the ellipse plate at Re = 1000 and $I^* = 0.08$.

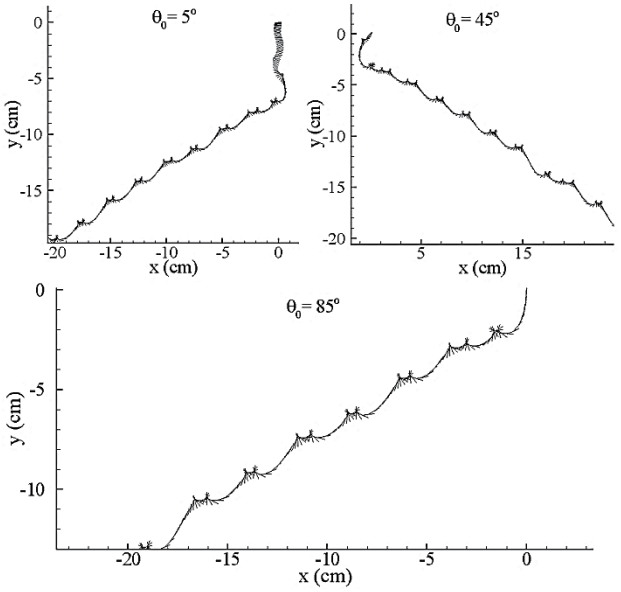


Fig. 7 The trajectories of the ellipse plate at Re = 1000 and $I^* = 0.35$.

4.3.1 Regime A: Steady falling

Steady falling looks like a needle falling in honey with small oscillation angles and almost straight downward to the bottom of a cup as shown in Fig. 5. As Fig. 4 shown, it occurs at the smaller Reynolds numbers, Re ≤ 50 ~ 100, depending on I^*. The center of mass of the ellipse is almost falling down straightforward to the bottom and two counter-rotating vortices appear behind the tails of the flat plate. Sometimes, it falls steadily with slightly oscillation due to the vortex shedding as shown in Figs. 10.

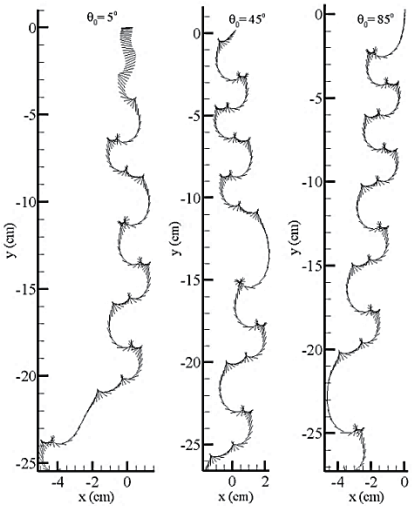


Fig. 8 The trajectories of the ellipse plate at Re = 1000 and $I^* = 0.25$.

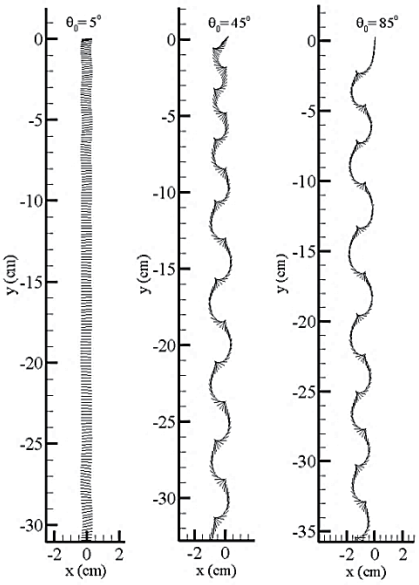


Fig. 9 The trajectories of the ellipse plate at Re = 100 and $I^* = 0.25$.

4.3.2 Regime B: Fluttering

Fluttering looks like a pirate boat swinging with large oscillation angles and side to side periodically to the ground as shown in Fig. 6. According to Fig. 4, it often happens at smaller dimensionless moment of inertia, $I^* < 0.12$ and larger Reynolds number, Re > 200. When the flat plate flutters side-to-side periodically, it reaches the extreme of its motion at the maximum incline angle θ_{max} as the angular velocity Ω equals to zero. Table 5 shows the collection of the maximum inclined angle θ_{max} for different Re, I^*, and θ_0, where θ_{max} is equal to the average of the maximum inclined angle during 10 period of side-to-side. At Table 5, we gather the high Reynolds number case with Re ≥ 1000 and find that the relation between I^* and $\overline{\theta}_{max}$ is almost linear increasing in Fig. 13. When θ_{max} is larger than 90°, it will enter to the transition regime between fluttering and tumbling regime or chaotic regime according to Fig. 4 shown.

https://doi.org/10.1017/jmech.2015.47 Published online by Cambridge University Press

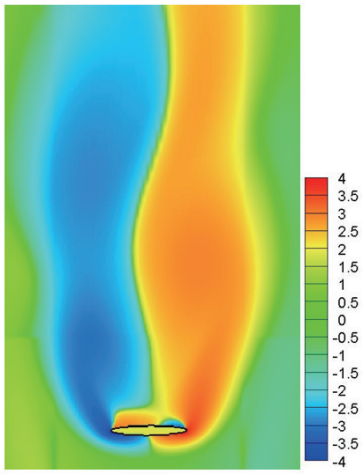


Fig. 10 The vorticity contours at an instantaneous time for the steady falling with Re = 100, $I^* = 0.08$, and $\theta_0 = 45°$.

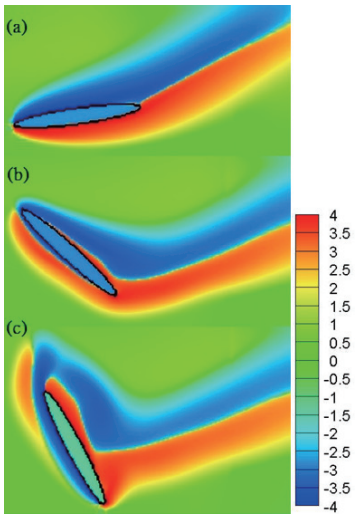


Fig. 11 The vorticity contours of three simple motion for the fluttering falling with Re = 1000, $I^* = 0.08$, and $\theta_0 = 45°$. (a) gliding downward; (b) center of mass elevation; (c) rotate to the side.

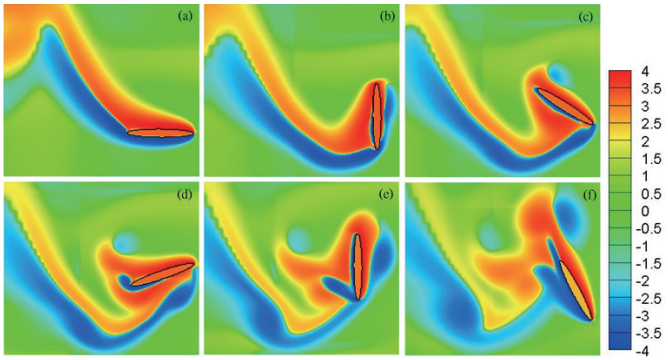


Fig. 12 The vorticity around the tumbling plate with Re = 1000, $I^* = 0.35$, and $\theta_0 = 45°$. (a) long gliding with center of mass elevation; (b) turn over; (c) ~ (d) short gliding without center of mass elevation; (e) turn over; (f) the plate resumes gliding.

Table 5 The collection of the maximum incline angle θ_{max} (deg) for different Re, I^* and θ_0 (deg).

I^*	Re	θ_{max} ($\theta_0 = 5$)	θ_{max} ($\theta_0 = 45$)	θ_{max} ($\theta_0 = 85$)	$\bar{\theta}_{max}$
0.08	1000	61.26	61.97	62.15	61.79
	2000	62.72	62.92	63.16	62.93
	5000	63.01	63.11	63.26	63.13
	10000	63.10	63.21	63.30	63.20
0.09	1000	67.80	68.27	68.34	68.14
	2000	69.06	69.22	69.24	69.17
	5000	69.24	69.26	69.30	69.27
	10000	69.37	69.37	69.33	69.36
0.10	1000	74.44	74.65	74.79	74.63
	2000	75.68	75.74	76.00	75.81
	5000	77.50	77.66	77.66	77.61
	10000	78.37	78.38	78.31	78.35
0.11	1000	82.41	82.71	83.00	82.71
	2000	84.30	84.21	84.18	84.23
	5000	84.44	85.13	84.97	84.85
	10000	85.84	85.47	85.65	85.65

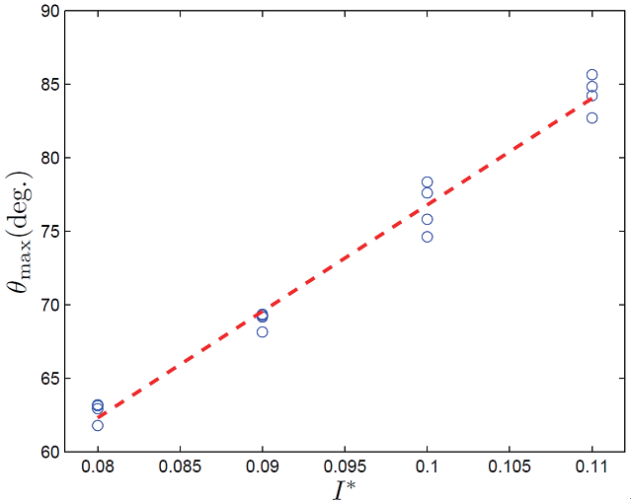


Fig. 13 The $I^*-\theta_{max}$ plot of the fluttering regime with $0.08 \le I^* \le 0.11$ and $1000 \le \mathrm{Re} \le 10000$.

Furthermore, two extreme cases for the fluttering motion are chosen from Table 5 to be discussed in detail. Under the same Re = 10000 and $\theta_0 = 45°$, the case of $I^* = 0.08$ reaches the maximum incline angle $\theta_{max} = 63.21°$ and the other case of $I^* = 0.11$ reaches $\theta_{max} = 85.47°$ approximate to vertical. Figures 14 and 15 display the variations of position, velocity and kinetic energy of their mass center during two times side-to-side oscillation. In these three plots, the blue color spot denotes the vertical velocity V is equal to zero and represents the extremum of center of mass elevation, and the red spot denotes zero angular velocity Ω and indicates θ approaches θ_{max}. The fluttering motion can be decomposed as three simple motions: (1) glide downward (from red to blue) (2) center of mass elevation (from blue to blue) (3) rotate to the side (from blue to red). In Figs. 14 and 15, their energy plots

https://doi.org/10.1017/jmech.2015.47 Published online by Cambridge University Press

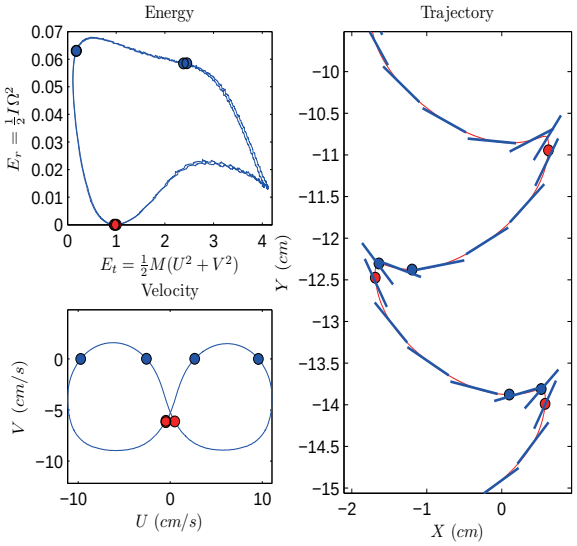


Fig. 14 The plots of trajectory, velocity and energy for $I^* = 0.08$, Re = 10000 and $\theta_0 = 45°$ in one period.

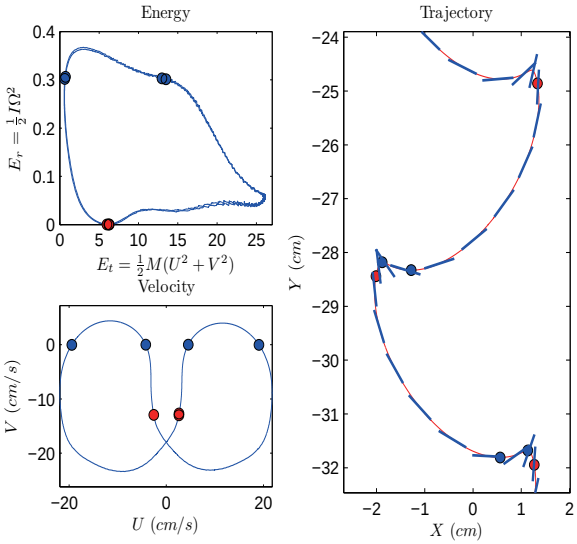


Fig. 15 The plots of trajectory, velocity and energy for $I^* = 0.11$, Re = 10000 and $\theta_0 = 45°$ in one period.

both draw a beak during gliding downward. The difference between them is that the later has straighter beak since it glide from larger initial inclined angle. As Fig. 11 shown, the upper and lower boundary layers are both thickened during gliding downward until the center of mass elevation. After the trailing edge becomes the leading edge, the lower boundary layer is cut off and the vorticity is shedding from the upper boundary layer.

4.3.3 Regime C: Tumbling

Tumbling looks like an eagle gliding in the sky with quick turning angle as shown in Fig. 7. Pesavento and Wang [9] pointed that, during the glide, the ellipse pitches up due to the fluid torque and slows down due to the increased drag. The small translational velocity results in a cusp-like shape around the turning points.

From Fig. 4, tumbling motion occurs principally at larger dimensionless moment of inertia, $I^* \geq 0.35$ and larger Reynolds number, Re ≥ 200. Sometimes, it also occurs in chaotic regime at some initial inclined angle θ_0. When the flat plate tumbles end-over-end periodically, it glides from one inclined vertical angle to another one. Table 6 shows the collection of the tumbling frequency f for different Re, I^*, and θ_0, where f is equal to the reciprocal of the average period during ten times end-over-end tumbling. At Table 6, we gather the high Reynolds number case with Re ≥ 1000 and find that I^* and $\bar{f}$ have a positive trend in Fig. 16.

Similarly, two extreme cases for the tumbling motion are chosen from Table 6 to be discussed in detail. Under the same Re = 10000 and $\theta_0 = 45°$, the cases of $I^* = 0.35$ and $I^* = 0.60$ rotate with frequencies $f = 14.33$ and $f = 18.40$, respectively. Figures 17 and 18 display the variations of position, velocity and kinetic energy of their mass center during two times end-over-end tumbling, respectively. In these three plots, the red spot denotes that the flat plate reach $\theta = 90°$ after the glide motion and also indicates the initial inclined angle of the next glide.

A casual observer of tumbling motion might notice that the lower I^* case sometimes consists of short and long gliding segments by turns as Fig. 17 shown and that the centre of mass only elevates after enough long glide time. Different to fluttering, the tumbling motion draw a smooth circle both on the energy and velocity plots for every gliding motion as Fig. 18 shown, but a simple knot for short gliding segment as Fig. 17 shown. No matter how the flat plate glides, it has less translational kinetic energy when reaching $\theta = 90°$ and turning over. As Fig. 12 shown, the vorticity variation during long gliding is similar to the gliding motion of fluttering falling and the vorticity is shedding after short gliding.

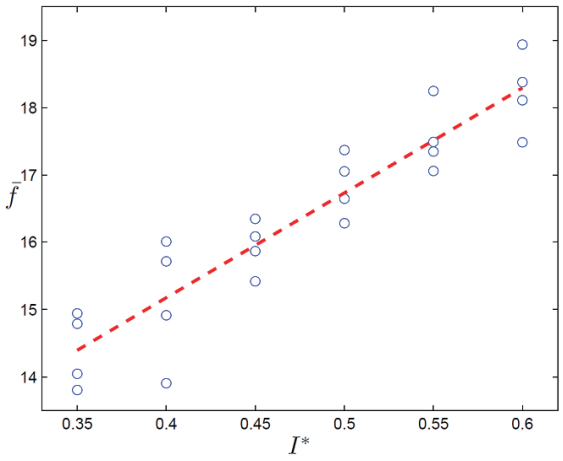


Fig. 16 The $I^* - \bar{f}$ plot of the tumbling regime with $0.35 \leq I^* \leq 0.60$ and $1000 \leq \mathrm{Re} \leq 10000$.

https://doi.org/10.1017/jmech.2015.47 Published online by Cambridge University Press

Table 6 The collection of the rotational frequency f for different Re, I^* and θ_0 (deg).

I^*	Re	f ($\theta_0=5$)	f ($\theta_0=45$)	f ($\theta_0=85$)	$\overline{f}$
0.35	1000	13.03	14.46	13.92	13.80
	2000	13.87	13.03	15.24	14.05
	5000	17.43	13.86	13.54	14.94
	10000	13.98	14.33	16.05	14.79
0.40	1000	14.16	13.71	13.84	13.90
	2000	14.33	14.44	15.97	14.91
	5000	16.07	16.37	14.70	15.71
	10000	16.77	16.47	14.79	16.01
0.45	1000	16.96	14.76	16.54	16.09
	2000	15.40	15.45	15.41	15.42
	5000	17.51	15.77	15.75	16.34
	10000	15.90	15.86	15.84	15.87
0.50	1000	16.27	17.37	17.53	17.06
	2000	16.27	16.28	16.29	16.28
	5000	16.64	16.67	16.62	16.64
	10000	18.62	16.76	16.73	17.37
0.55	1000	17.23	16.43	18.37	17.34
	2000	17.07	17.05	17.06	17.06
	5000	17.50	17.52	17.46	17.49
	10000	17.60	17.61	19.53	18.25
0.60	1000	18.11	17.12	17.22	17.48
	2000	18.76	17.77	17.81	18.11
	5000	18.21	20.34	18.26	18.94
	10000	18.36	18.40	18.37	18.38

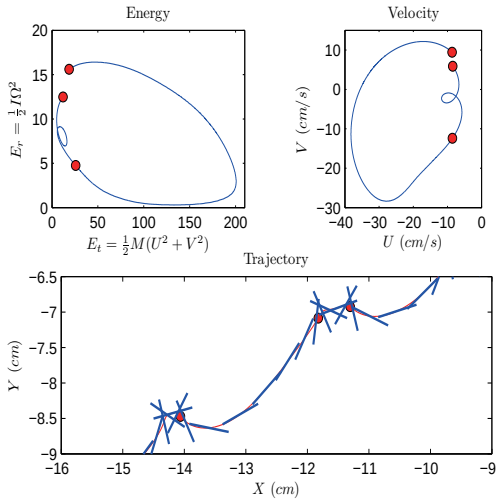


Fig. 17 The plots of trajectory, velocity and energy for $I^* = 0.35$, Re = 10000 and $\theta_0 = 45°$ in one period.

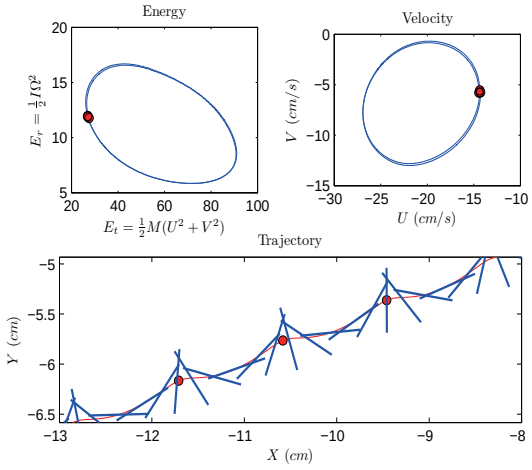


Fig. 18 The plots of trajectory, velocity and energy for $I^* = 0.60$, Re = 10000 and $\theta_0 = 45°$ in one period.

5. CONCLUSIONS

A modified direct-forcing IB pressure correction method has been developed to simulate the flows of a falling ellipse. The direct forcing method to capture the particle velocity is introduced in the IB method. The index function is defined to describe the configuration of a particle. By using the direct forcing method and Gaussian theorem, the formulas for computing the hydrodynamic force and torque acting on the particle are derived from the volume integrals. For the simulations of the flows past a fixed ellipse, the method computes the drag force very well. The simulation of freely falling flat plate coincide with the experiment. The Re-I^* phase diagram is established to classify the types of the behavior of the falling ellipse.

As can be seen from Fig. 4, the falling behavior change from steady falling to tumbling in the sequence: Regime A→D→B→E→C. The falling behavior is dominated by the viscous effect in regime A and D, and by the rotational motion in regime B, E and C. From regime D to A, the flutter motion turns into the steady falling. From regime B to E and C in order, the flutter motion turns into the tumbling motion. In addition, the initial incline angle θ_0 influence initial rotational energy, but it only affects the borderline case like the regime D and E, as the Figs. 9 and 8 shown, respectively. In regime B, Fig. 13 shows that the maximum incline angle $\theta_{\max}$ is almost linear increasing by I^* and an overturn motion appear while the incline angle achieve 90 degrees. In regime C, the Fig. 16 indicate that the tendency to tumble frequency f increases with I^*.

ACKNOWLEDGEMENTS

The authors wish to extend their appreciation for the supports awarded by the National Science Council of the Republic of China under the contact NSC 100-2221-E-006-106.

REFERENCES

1. Andersen, A., Pesavento U. and Wang Z. J., "Unsteady Aerodynamics of Fluttering and Tumbling Plates," *Journal of Fluid Mechanics*, **541**, pp. 65–90 (2005).
2. Andersen, A., Pesavento, U. and Wang, Z. J., "Analysis of Transitions Between Fluttering, Tumbling and Steady Descent of Falling Cards," *Journal of Fluid Mechanics*, **541**, pp. 91–104 (2005).
3. Jin, C. and Xu, K., "Numerical Study of the Unsteady Aerodynamics of the Freely Falling Plates," *Communications in Computational Physics*, **3**, pp. 834–851 (2008).
4. Kolomenskiy, D. amd Schneider, K., "Numerical Simulations of Falling Leaves Using a Pseudo-Spectral Method with Volume Penalization," *Theoretical and Computational Fluid Dynamics*, **24**, pp.

https://doi.org/10.1017/jmech.2015.47 Published online by Cambridge University Press

169–173 (2010).
5. Smith, E. H., "Autorotating Wings: An Experimental Investigation," *Journal of Fluid Mechanics*, **50**, pp. 513–534 (1971).
6. Tanabe, Y. and Kaneko, K., "Behavior of a Falling Paper," *Physical Review Letters*, **73**, pp. 1372–1421 (1994).
7. Belmonte, A., Eisenberg, H. and Moses, E., "From Flutter to Tumble: Inertial Drag and Frounde Similarity in Falling Paper," *Physical Review Letters*, **81**, pp. 345–348 (1998).
8. Mahadevan, L., Ryu, W. S. and Samuel, A. D. T., "Tumbling Cards," *Physics Fluids*, **11**, 111070–6631/11(1) (1999).
9. Pesavento, U. and Wang, Z. J., "Falling Paper: Navier-Stokes Solutions, Model of Fluid Forces, and Center of Mass Elevation," *Physical Review Letters*, **93**, 144501 (2004).
10. Haeri, S. and Shrimpton, J. S., "On the Application of Immersed Boundary, Fictitious Domain and Body-Conformal Mesh Methods to Many Particle Multiphase Flows," *International Journal of Multiphase Flow*, **40**, pp. 38–55 (2012).
11. Hu, H., "Direct Simulation of Flows of Solid-Liquid Mixtures," *International Journal of Multiphase Flow*, **22**, pp. 332–335 (1996).
12. Johnson, A. A. and Tezduyar, T. E., "Simulation of Multiple Spheres Falling in a Liquid-Filled Tube," *Computer Methods in Applied Mechanics and Engineering*, **134**, pp. 351–373 (1996).
13. Johnson, A. A. and Tezduyar, T. E., "Advanced Mesh Generation and Update Methods for 3D Flow Simulations," *Computational Mechanics*, **23**, pp. 130–143 (1999).
14. Hu, H., Joseph, D. and Crochet, M., "Direct Simulation of Fluid Particle Motions," *Theoretical and Computational Fluid Dynamics*, **3**, pp. 285–306 (1992).
15. Gan, H., Chang, J., Feng, J. and Hu, H., "Direct Numerical Simulation of the Sedimentation of Solid Particles with Thermal Convection," *Journal of Fluid Mechanics*, **481**, pp. 385–411 (2003).
16. Johnson, A. and Tezduyar, T., "Models for 3D Computations of Fluid-Particle Interactions in Spatially Periodic Flows," *Computer Methods in Applied Mechanics and Engineering*, **190**, pp. 3201–3221 (2001).
17. Wan, D. and Turek, S., "Direct Numerical Simulation of Particulate Flow via Multigrid FEM Techniques and the Fictitious Boundary Method," *International Journal for Numerical Methods in Fluids*, **51**, pp. 531–566 (2006).
18. Wan, D. and Turek, S., "Fictitious Boundary and Moving Mesh Methods for the Numerical Simulation of Rigid Particulate Flows," *Journal of Computational Physics*, **222**, pp. 28–56 (2007).
19. Peskin, C. S., "Numerical Analysis of Blood Flow in the Heart," *Journal of Computational Physics*, **25**, pp. 220–252 (1977).
20. Höfler, K. and Schwarzer, S., "Navier-Stokes Simulation with Constraint Forces: Finite-Difference Method for Particle-Laden Flows and Complex Geometries," *Physical Review E*, **61**, pp. 7146–7160 (2000).
21. Feng, Z. G. and Michaelides, E. E., "The Immersed Boundary-Lattice Boltzmann Method for Solving Fluid-Particles Interaction Problems," *Journal of Computational Physics*, **195**, pp. 602–628 (2004).
22. Lai, M. C. and Peskin, C., "An Immersed Boundary Method with Formal Second-Order Accuracy and Reduced Numerical Viscosity," *Journal of Computational Physics*, **160**, pp. 705–719 (2000).
23. Lee, C., "Stability Characteristics of the Virtual Boundary Method in Three-Dimensional Applications," *Journal of Computational Physics*, **184**, pp. 559–591 (2003).
24. Fadlun, E. A., Verizicco, R., Orlandi, P. and Mohd-Yusof, J., "Combined Immersed-Boundary Finite-Difference Methods for Three-Dimensional Complex Flow Simulations," *Journal of Computational Physics*, **161**, pp. 35–60 (2000).
25. Feng, Z. G. and Michaelides, E. E., "Proteus: A Direct Forcing Method in the Simulations of Particulate Flows," *Journal of Computational Physics*, **202**, pp. 20–51 (2005).
26. Uhlmann, M., "An Immersed Boundary Method with Direct Forcing for the Simulation of Particulate Flows," *Journal of Computational Physics*, **209**, pp. 448–476 (2005).
27. Lin, S. Y., Chin, Y. H., Hu, J. J. and Chen, Y. C., "A Pressure Correction Method for Fluid-Particle Interaction Flow: Direct Forcing Method and Sedimentation Flow," *International Journal for Numerical Methods in Fluids*, **67**, pp. 1171–1798 (2011).
28. Dennis, S. C. R. and Chang, G. Z., "Numerical Integration of the Navier-Stokes Equations for Steady Two-Dimensional Flow," *Physics of Fluids*, **12**, pp. 88–93 (1969).
29. Lugt, H. J. and Haussling, H. J., "Laminar Flows Past Elliptic Cylinders at Various Angles of Attack," *Naval Ship Research and Development Center*, **3748** (1972).
30. Mittal, R., Seshadri, V., Udaykumar, H. S., "Flutter, Tumble and Vortex Induced Autorotation," *Theoretical and Computational Fluid Dynamics*, **17**, pp. 165–170 (2004).

(Manuscript received November 7, 2014,
accepted for publication January 26, 2015.)

https://doi.org/10.1017/jmech.2015.47 Published online by Cambridge University Press